

High-performance supercapacitors based on Ni₂P@CNT nanocomposites prepared using an ultrafast microwave approach

Yunrui Tian¹, Haishun Du², Shatila Sarwar², Wenjie Dong¹, Yayun Zheng¹, Shumin Wang¹, Qingping Guo¹,
Jujie Luo (✉)¹, Xinyu Zhang (✉)²

¹ College of Materials Science and Engineering, Taiyuan University of Technology, Taiyuan 030024, China
² Department of Chemical Engineering, Auburn University, Auburn, AL 36849, USA

© Higher Education Press 2020

Abstract We present a one-step route for the preparation of nickel phosphide/carbon nanotube (Ni₂P@CNT) nanocomposites for supercapacitor applications using a facile, ultrafast (90 s) microwave-based approach. Ni₂P nanoparticles could grow uniformly on the surface of CNTs under the optimized reaction conditions, namely, a feeding ratio of 30:50:25 for CNT, Ni(NO₃)₂·6H₂O, and red phosphorus and a microwave power of 1000 W for 90 s. Our study demonstrated that the single-step microwave synthesis process for creating metal phosphide nanoparticles was faster and simpler than all the other existing methods. Electrochemical results showed that the specific capacitance of the optimal Ni₂P@CNT-nanocomposite electrode displayed a high specific capacitance of 854 F·g⁻¹ at 1 A·g⁻¹ and a superior capacitance retention of 84% after 5000 cycles at 10 A·g⁻¹. Finally, an asymmetric supercapacitor was assembled using the nanocomposite with activated carbon as one electrode (Ni₂P@CNT//AC), which showed a remarkable energy density of 33.5 W·h·kg⁻¹ and a power density of 387.5 W·kg⁻¹. This work will pave the way for the microwave synthesis of other transition metal phosphide materials for use in energy storage systems.

Keywords Ni₂P, CNT, supercapacitors, nanocomposites, microwave

1 Introduction

The development of advanced energy storage technology has become a major research focus because of the limitations posed by fossil fuel resources [1–5]. Recently,

supercapacitors have emerged as promising energy storage devices and have drawn extensive interest because of their strong cycle stability and high power density. Supercapacitors can be divided into three categories based on the energy storage mechanism they employ: electrochemical double-layer capacitors, pseudo-capacitors, and hybrid supercapacitors (HSCs). Among them, HSCs are the first choice for high-power and high-energy electrochemical energy storage devices [6–9]. The electrochemical performance of HSCs depends to a large extent on the composition of electrode materials. Therefore, the selection of the efficient electrode materials is important for the development of advanced supercapacitor devices [10–13].

In recent years, transition metal phosphides have emerged as novel electrode materials for high-performance asymmetric supercapacitors (ASCs) [14,15]. As N-type semiconductors, transition metal phosphides have superior electrical conductivity and low polarization [16]. Moreover, transition metal phosphides form open frameworks with large channels inside their structures, which makes them kinetically favorable for fast ion/electron transfer [17,18]. Among them, Ni₂P is considered one of the most promising electrode materials for supercapacitors because of its high theoretical capacity (1951.2 C·g⁻¹) [19,20]. Nonetheless, Ni₂P has poor rate capability and cycling performance [21,22]. One effective approach to overcome this drawback is to hybridize Ni₂P with highly conductive materials, such as carbon-based materials [23]. This idea has been explored in a large number of studies [19,24]. For example, Liu et al. reported the synthesis of reduced graphene oxide/nickel phosphide (rGO/Ni₂P) composites via an *in-situ* phosphorization process and found that the rGO/Ni₂P composite electrode has the highest specific capacitance among the materials tested with a capacitance of 890 F·g⁻¹ at 1 A·g⁻¹ [24]. Hou et al. synthesized carbon-

incorporated Janus-type Ni₂P/Ni hollow spheres (Ni₂P/Ni/C), which showed a very high specific capacitance of 1499 F·g⁻¹ at 1 A·g⁻¹ [20]. We were encouraged by these promising findings; thus, we predicted that the electrochemical performance and stability of Ni₂P@CNT nanocomposites will be remarkably improved over that of base Ni₂P.

Current studies on the synthesis of Ni₂P/carbon composites are limited to traditional methods, such as hydrothermal technology [25], *in-situ* processing [26], thermal decomposition synthesis [27], and wet chemical-based reduction [28]. These methods require a long synthesis time and harsh synthesis conditions and waste a lot of manpower and material resources. Compared with traditional methods of temperature control, microwave heating converts energy through dipole rotation and ion conduction inside materials; thus, it has the advantages of rapidity, selectivity, and uniformity [29]. Given these advantages, a large number of different electrode materials are prepared using microwave heating [30,32]. In addition, the microwave synthesis process for nanocomposites does not need gas protection, is simple to perform, and requires no pretreatment, which are all necessary for the industrial application of the synthesis technique.

Herein, we demonstrated the fabrication of Ni₂P@CNT nanocomposites for HSC applications by a one-step, ultrafast microwave synthesis (Scheme 1). The uniform growth of Ni₂P nanospheres on the surface of the CNTs was achieved by transient microwave radiation (e.g., 90 s). The experimental parameters, including microwave power,

heating time, and precursor mass ratio were optimized, and the surface chemistry, crystalline structure, and morphology of the as-produced nanocomposites were characterized by Fourier-transform infrared (FTIR) spectrometry, X-ray diffraction (XRD), X-ray photoelectron spectroscopy (XPS), energy-dispersive X-ray spectroscopy (EDS), Brunner-Emmet-Teller measurements (BET), and scanning electron microscopy (SEM) analyses. Moreover, the electrochemical behaviors of the as-prepared nanocomposites were examined by cyclic voltammetry (CV), chronopotentiometry (CP), and electrochemical impedance spectroscopy (EIS). An asymmetric supercapacitor was assembled by employing the Ni₂P@CNT nanocomposites as the positive electrode and activated carbon (AC) as the negative electrode to investigate its electrochemical performance and explore its practical application.

2 Experimental

2.1 Materials

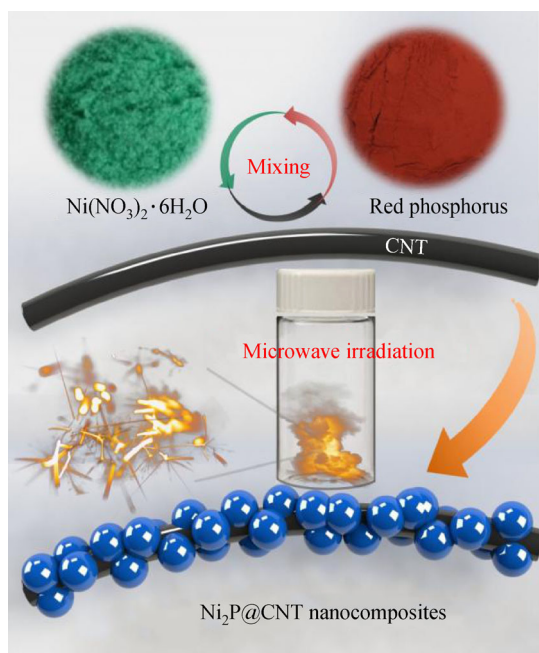
Nickel nitrate hexahydrate (Ni(NO₃)₂·6H₂O) was obtained from Sinopharm Chemical Reagent Co., Ltd. CNTs were purchased from Chengdu Organic Chemicals Co., Ltd. Red phosphorus and acetylene black were obtained from Aladdin Co. The rest of the raw materials came from Tianjin Damao Co.

2.2 Synthesis of Ni₂P@CNT nanocomposites

CNTs (30 mg), red phosphorus (25 mg), and Ni(NO₃)₂·6H₂O (50 mg) were mixed evenly to obtain a fine powder. The resulting powder mixture was transferred to a microwave oven (Panasonic NN-GF352M, 2450 MHz, 1000 W) for irradiation. Reaction parameters in terms of the mass ratio of CNT and precursors, radiation time, and microwave power were designed to achieve optimal Ni₂P@CNT nanocomposites. All the relevant information is given in Table 1.

2.3 Material characterization

The morphology of the as-prepared nanocomposites was characterized by SEM (TSCAN Mira 3 LMH) and high-resolution transmission electron microscopy (HRTEM, JEM-2100F). The elementary composition of the nanocomposites was determined by EDS analysis using the scanning electron microscope. These results were further supported by FTIR (Bruker Tensor II). The crystalline structure was characterized by XRD (Rigaku D/max-2500). The specific surface area of the nanocomposites was analyzed by BET (ASAP 2020). In addition, XPS (Thermo Scientific Escalab250Xi) was used to determine the elemental valence states of the obtained nanocomposite samples.



Scheme 1 Schematic diagram of microwave initiated Ni₂P nanosphere growth on graphite CNT.

Table 1 Operation conditions for synthesizing Ni₂P@CNT nanocomposites

Sample	C:N:P	C ^a /mg	N ^b /mg	P ^c /mg	Microwave power/W	Heating time/s
a	30:50:25	30	50	25	1000	60
b	30:50:25	30	50	25	1000	90
c	30:50:25	30	50	25	1000	120
d	30:50:25	30	50	25	800	90
e	30:40:20	30	40	20	1000	90
f	30:60:30	30	60	30	1000	90

a): CNT; b): Ni(NO₃)₂·6H₂O; c): red phosphorus.

2.4 Electrochemical measurements

The electrochemical properties of the resultant Ni₂P@CNT nanocomposites were studied in an aqueous 6 mol·L⁻¹ KOH solution using a three-electrode system. Platinum foil and mercury/mercury oxide (RO501) electrodes were used as the counter electrode and reference electrode, respectively. The working electrodes were prepared using the traditional slurry coating process. First, the nanocomposites were mixed with acetylene black and polyvinylidene fluoride at a weight ratio of 8:1:1. Second, the mixed material was coated onto a nickel foam surface (1 cm × 1 cm) while maintaining an active material loading mass of approximately 1 mg. Finally, the nickel foam with slurry coating was dried at 80 °C for 24 h to remove the solvent. The electrochemical behaviors of the as-prepared nanocomposite electrodes were measured by CV, CP, and EIS. The specific capacitance of the Ni₂P@CNT nanocomposite was calculated from the following equation:

$$C = (I \times \Delta t) / (\Delta V \times m), \quad (1)$$

where C is the specific capacitance (F·g⁻¹), I is the current (A), m is the mass of active material (mg), ΔV is the potential range (V), and Δt is discharge time (s).

In addition, an ASC system (Ni₂P@CNT//AC) was assembled using the Ni₂P@CNT nanocomposites as the positive electrode and AC (The electrochemical performance is shown in Fig. S7, cf. Electronic Supplementary Material (ESM)) as the negative electrode. The energy and power densities were calculated from the following equations:

$$E = C\Delta V^2 / (2 \times 3.6), \quad (2)$$

$$P = 3600 \times E / \Delta t, \quad (3)$$

where E is the energy density (W·h·kg⁻¹) and P is the power density (kW·kg⁻¹). ASC was prepared using 6 mol·L⁻¹ KOH as electrolyte and Ni₂P@CNT and AC as positive and negative electrode materials, respectively. The optimum mass ratio of the positive and negative electrodes was obtained by the following equation:

$$m^+ / m^- = C^- \Delta V^- / C^+ \Delta V^+. \quad (4)$$

The mass ratio of the positive and negative materials was maintained at 0.45.

3 Results and discussion

3.1 Chemical composition and surface elemental analysis

XRD, XPS, and FTIR characterizations were performed to determine the chemical composition and elemental state of the as-prepared Ni₂P@CNT nanocomposites. As shown in Fig. 1(a), compared with the XRD pattern of pure CNT, the XRD pattern of the Ni₂P@CNT nanocomposite has additional sharp and well-defined diffraction peaks, which could be assigned to the (111), (201), (210), (300), and (211) planes of Ni₂P (JCPDS No. 65-3544), demonstrating the generation of Ni₂P with a high-quality crystalline structure. However, as shown in Fig. 1(b), the diffraction peaks of Ni(NO₃)₂·6H₂O (JCPDS No. 74-0666) and red phosphorus (JCPDS No. 76-1957) were still visible and indicate incomplete reactions when the reaction time was shorter (sample a), the reaction power was lower (sample d), or when the feeding amount of Ni(NO₃)₂·6H₂O was too high (sample e). Figures 1(c) and 1(d) show the elemental compositions and valence states of the obtained Ni₂P@CNT nanocomposites. The two major peaks at 856.3 eV (satellite peak at 862.6 eV) and 874.9 eV (satellite peak at 880.9 eV) agree well with Ni 2p_{3/2} and 2p_{1/2}. For the P 2p spectrum, the peaks at 129.8 and 130.7 eV are assigned to the P 2p_{3/2} and P 2p_{1/2} states of metal phosphides, and the peak at 133.8 eV corresponds to P–O from surface oxidation [33,34]. All the above results indicated that Ni₂P was successfully synthesized using the one-step microwave approach. As shown in Fig. S6 (cf. ESM), the vibration spectra of the two samples are very similar except for the main difference observed in the range of 800–1500 cm⁻¹. This difference in peaks is attributed to the stretching vibration of the Ni–P bond, which confirms the successful synthesis of the Ni₂P@CNT nanocomposites.

3.2 Morphology and structure characterization

The surface morphologies of the resultant Ni₂P@CNT

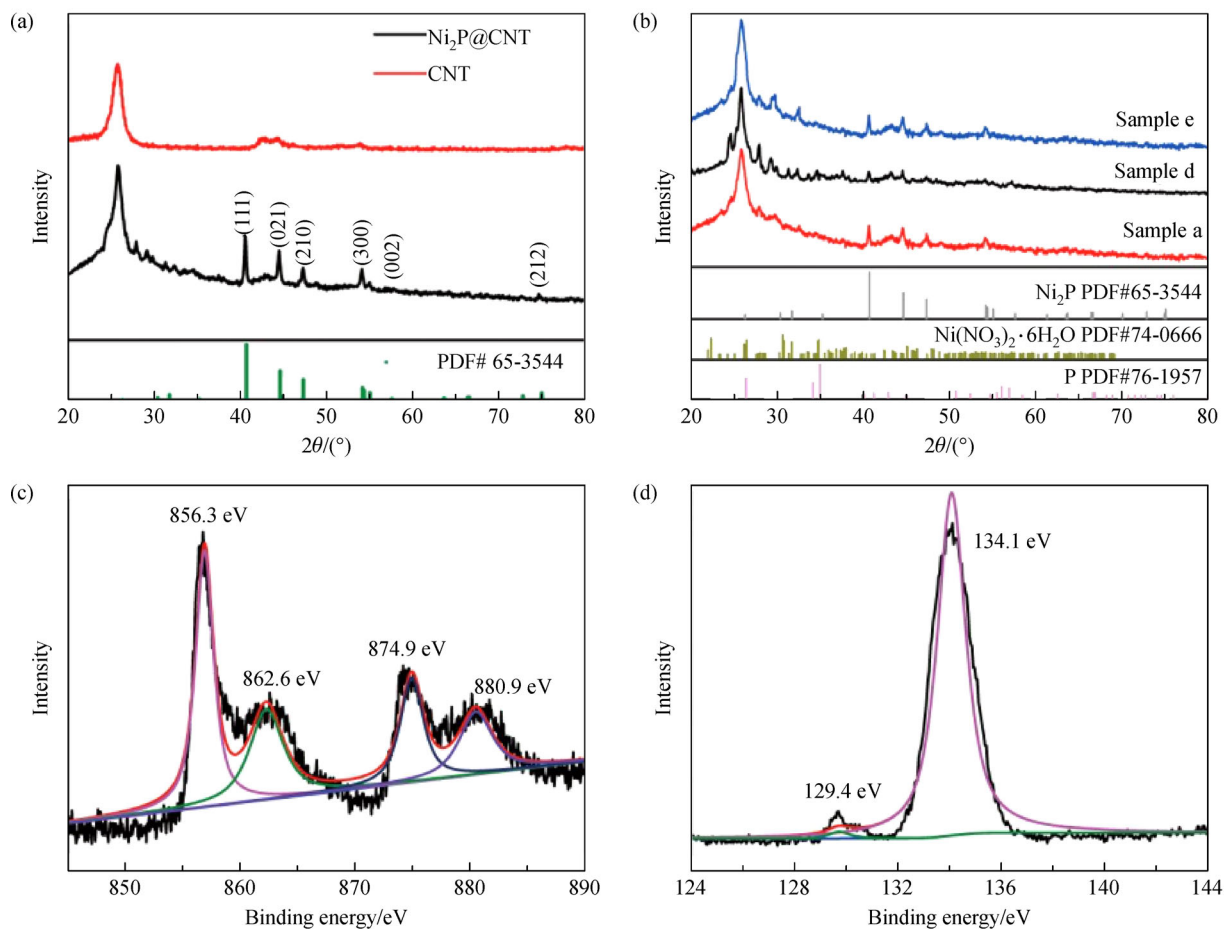


Fig. 1 Chemical composition and surface elemental analysis of CNTs and $\text{Ni}_2\text{P}@$ CNT nanocomposites: (a) XRD patterns of pure CNT and $\text{Ni}_2\text{P}@$ CNT (sample b); (b) XRD patterns of the samples under different experimental conditions; (c) XPS spectra of Ni (sample b); (d) XPS spectra of P (sample b).

nanocomposites were studied by SEM. As shown in Fig. 2(b), the Ni_2P nanospheres are evenly distributed on the CNT surface. This favorable morphology would be conducive to electron transfer; thus, the obtained $\text{Ni}_2\text{P}@$ CNT nanocomposites have potential as energy storage materials. The morphology of the other samples synthesized under different experimental conditions was also examined by SEM, and the results will be discussed in the following section. As shown in Fig. 2(g), the EDS spectrum confirmed that the synthesized $\text{Ni}_2\text{P}@$ CNT nanocomposite (sample b) was composed of C, Ni, and P. A small oxygen peak is present in the EDS spectrum. This peak was probably due to the fact that the surface of the CNT and Ni_2P nanoparticles became slightly oxidized at high temperatures during synthesis [35,37]. The percentage content of each element in the XPS and EDS tests is shown in Table S1 (cf. ESM).

The low-magnification TEM image shown in Fig. S1(a) (cf. ESM) shows that Ni_2P grew on the surface of CNT. This result was consistent with the SEM results. As shown in the HRTEM image in Fig. S1(b), the planar spacing of

the well-defined lattice stripes was 0.22 nm, which is consistent with the spacing of (111) crystals and corresponds to a hexagonal Ni_2P structure. The selected area electron diffraction pattern is shown in the inset of Fig. S1(b). The diffraction spots and diffraction rings corresponded to the nanoparticles of Ni_2P and CNTs, respectively, which is consistent with the HRTEM results. According to Fig. S2 (cf. ESM) and Table 2, the synthesized electrode materials have a good specific surface area, which can provide more active sites for electrochemical reactions.

3.3 Electrochemical properties after different fabrication conditions

As shown in Fig. 3 and Fig. S5 (cf. ESM), the electrochemical properties of the prepared $\text{Ni}_2\text{P}@$ CNT nanocomposite were optimized by adjusting the reaction parameters in terms of reaction time, microwave power, and the mass ratio of CNT to precursors. First, the effect of reaction time was investigated (samples a–c in Table 1). As

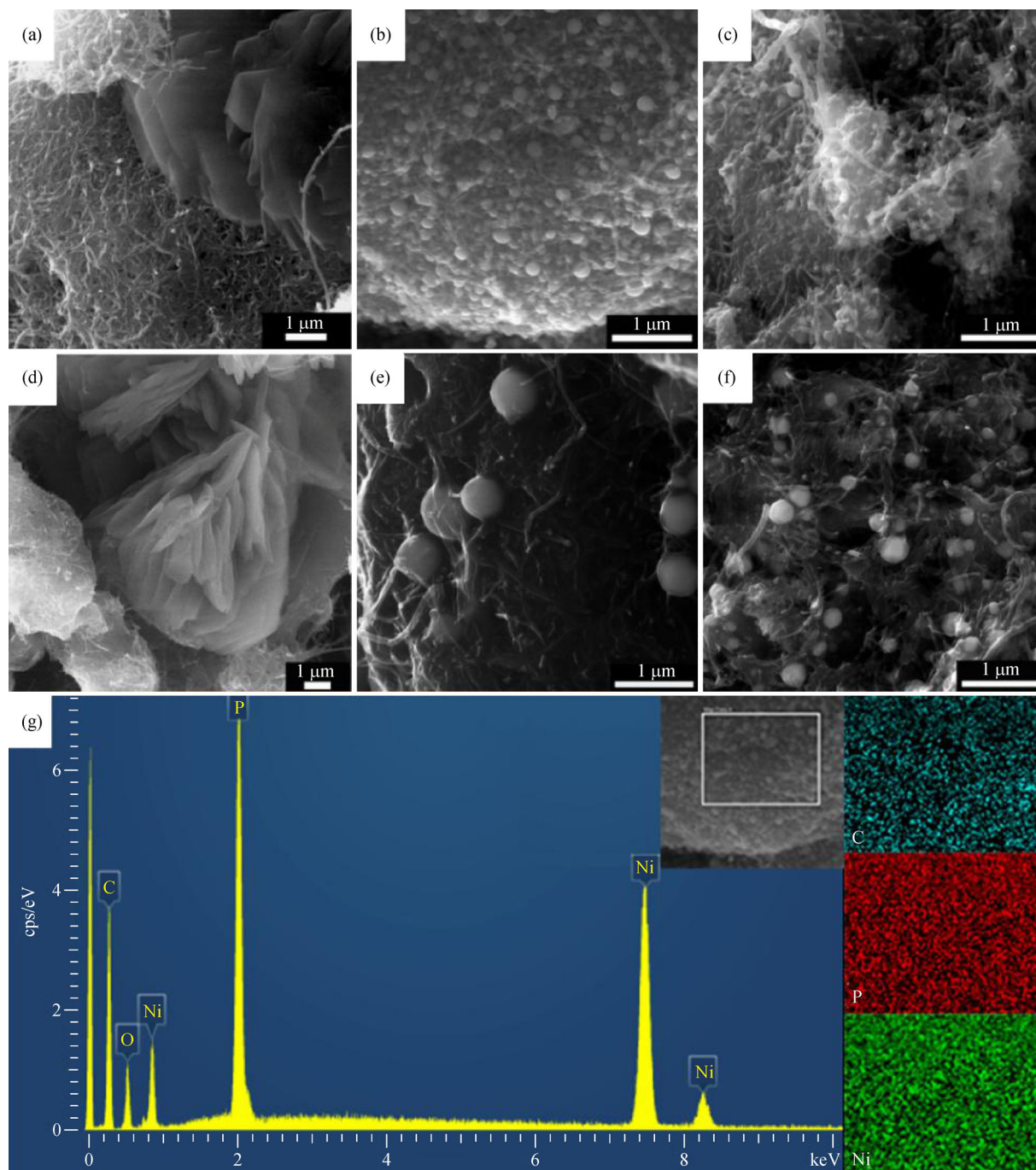


Fig. 2 SEM images of the as-prepared Ni₂P@CNT nanocomposites under different experimental conditions: (a) sample a; (b) sample b, (c) sample c; (d) sample d; (e) sample e; (f) sample f; (g) EDS images of sample b.

Table 2 Pore structural parameters and compositions of the samples

Sample	$S_{\text{BET}}/(\text{m}^2 \cdot \text{g}^{-1})$	$S_{\text{micro}}/(\text{m}^2 \cdot \text{g}^{-1})$	$V_{\text{total}}/(\text{cm}^3 \cdot \text{g}^{-1})$	$V_{\text{micro}}/(\text{cm}^3 \cdot \text{g}^{-1})$
Ni ₂ P@CNT	23.3832	1.1811	0.205434	0.000134

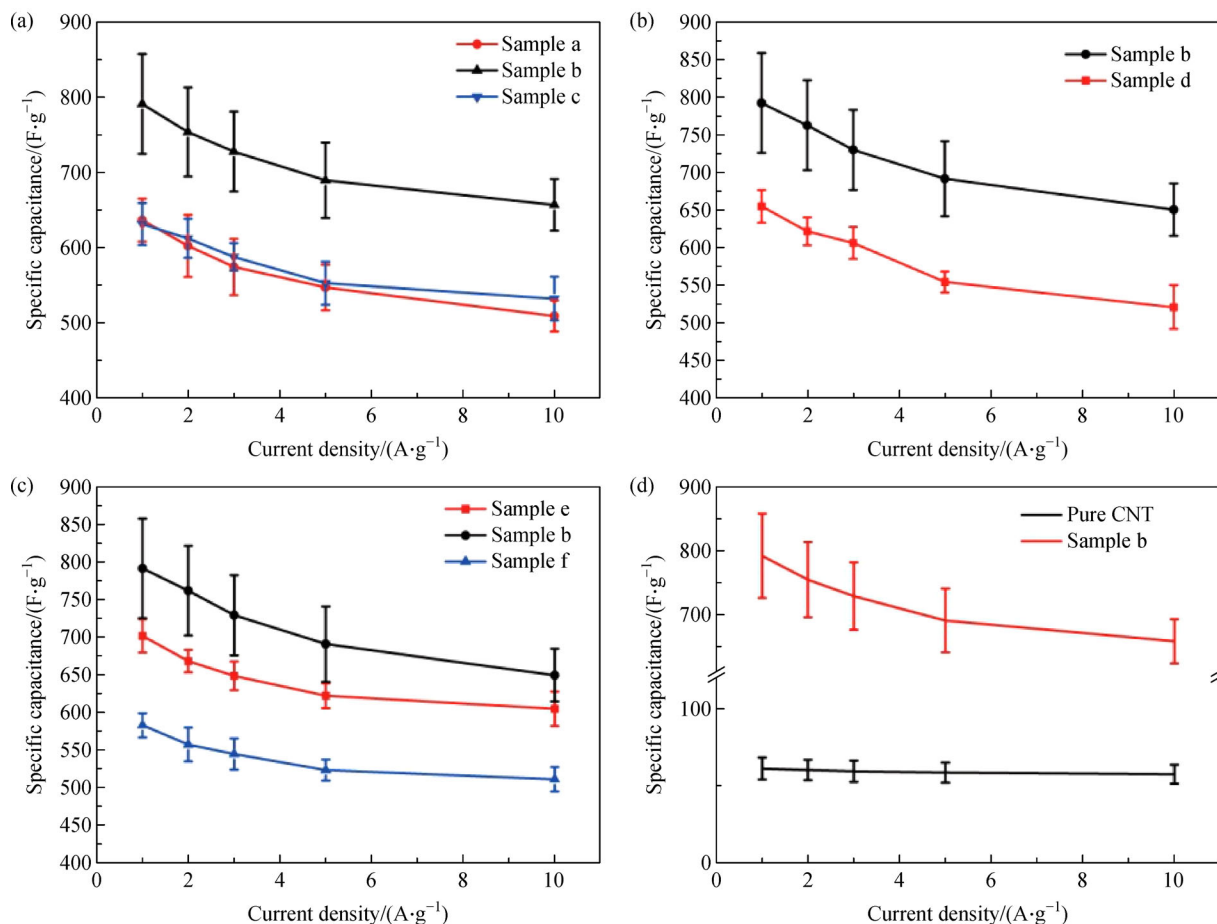


Fig. 3 Comparison of the specific capacitance values of the as-prepared Ni₂P@CNT nanocomposite under different experimental conditions: (a) reaction time; (b) reaction power; (c) feeding ratio of precursors to CNTs; (d) specific capacitance of sample b and pure CNTs at different current densities.

shown in the SEM images, only a small quantity of Ni₂P nanoparticles was generated within the relatively short reaction time of 60 s (Fig. 2(a)). Uniform Ni₂P nanoparticles were generated on the CNTs when the heating time was prolonged to 90 s (Fig. 2(b)). However, large agglomerates of Ni₂P nanoparticles were formed when the heating time was increased to 120 s as shown in Fig. 2(d) [38,39]. Correspondingly, sample b showed the highest specific capacitance, followed by samples c and a (Fig. 3(a)). The initially increased specific capacitance should be credited to the high theoretical specific capacitance of Ni₂P. Figure 3(d) clearly illustrates that the pure CNT exhibited a much smaller specific capacitance than the Ni₂P@CNT nanocomposites. The reduced specific capacitance for sample c was probably due to the nanoparticle agglomeration, which can impede ion insertion and transport, as well as reduce the surface area [32]. A slightly lower microwave power (800 W) was also tested in an attempt to synthesize the nanocomposite (sample d). However, Fig. 2(e) reveals that only a small quantity of Ni₂P nanoparticles was generated using this lower

microwave power, because the CNTs could not absorb enough heat to promote the generation of Ni₂P nanoparticles. Therefore, Fig. 3(b) shows a much smaller specific capacitance for sample d than for sample b. Finally, we kept the amount of CNTs constant and altered the quantity of the precursors added (Ni(NO₃)₂·6H₂O and red phosphorus). The mass ratio of Ni(NO₃)₂·6H₂O to red phosphorus was kept at 2:1 for all the samples based on the target product (Ni₂P). As shown in Fig. 3(c), the specific capacitance initially increased and then decreased as the quantity of precursors increased. The initially increased specific capacitance should be attributed to the increased Ni₂P content. Figure 2(f) shows that fewer Ni₂P nanoparticles were generated in sample e than in sample b. However, the water in Ni(NO₃)₂·6H₂O also increased with the increase of precursors for sample f and probably competed with the CNTs to absorb the microwave energy. This increase in water resulted in the incomplete transformation of the precursors to Ni₂P nanoparticles. The small quantity of Ni₂P nanoparticles in sample f (Fig. 2(f)) proved our speculation. Overall, the optimum

experimental conditions for the synthesis of Ni₂P@CNT nanocomposites were a feeding ratio of 30:50:25 for CNTs, Ni(NO₃)₂·6H₂O, and red phosphorus and a microwave power of 1000 W for 90 s as manifested by sample b.

3.4 Electrochemical properties in a three-electrode system

The CV curves of sample b were obtained at different scan rates ranging from 5 to 100 mV·s⁻¹ (Fig. 4(a)) in a three-electrode configuration to further evaluate the electrochemical performance of the as-prepared Ni₂P@CNT nanocomposites. The cathodic and anodic current responses of the Ni₂P@CNT nanocomposite were detected between 0 and 0.6 V. A distinct pair of redox peaks was observed in the CV curves and corresponds to the reversible faradaic reaction of Ni²⁺/Ni³⁺. The reversible electrode reaction of the Ni₂P@CNT nanocomposites in strong alkaline electrolytes can be described below [20].

Figure 4(b) exhibits the galvanostatic charge-discharge (GCD) curves measured between 0 and 0.5 V. According to the curves, the specific capacitance was calculated to be 854, 815, 779, 744 and 688 F·g⁻¹ at the current densities of 1, 2, 3, 5 and 10 A·g⁻¹, respectively. Figures S5(a) and S5(c) show that the CV curve area of sample b is the largest and its GCD curve discharge time is the longest; hence, the electrochemical performance of sample B is the best among the samples [5,40]. We further carried out EIS measurements at frequencies ranging from 100 kHz to 0.01 Hz. As shown in Fig. 4(c), the Nyquist plot of the Ni₂P@CNT nanocomposite is composed of a semicircle, which decreases in the high-frequency region and forms a straight line in the low-frequency region. The slope of the curve in the low-frequency region is related to the capacitive behavior of the supercapacitor [4,41]. In Fig. S5(b), the curve slope of sample b in the low-frequency region is larger, which indicates that sample b has a more ideal capacitance behavior. The ohmic

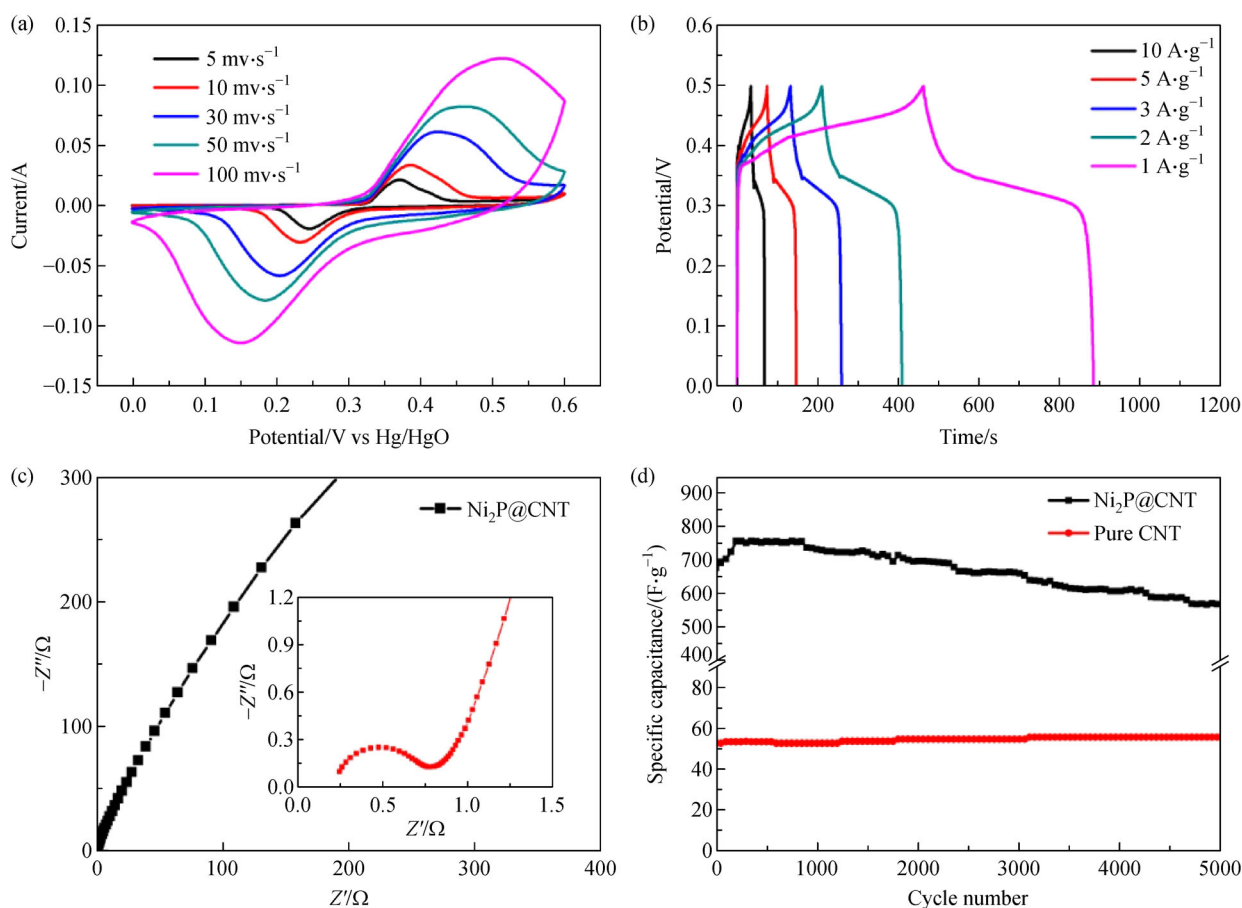


Fig. 4 (a) CV curves of a Ni₂P@CNT nanocomposite (sample b) at different scan rates from 5–100 mV·s⁻¹; (b) GCD curves at current densities of 1–10 A·g⁻¹; (c) Nyquist plots of a Ni₂P@CNT nanocomposite (sample b), inset shows x-axis range from 0 to 1.5 Ω; (d) cycling stability of a Ni₂P@CNT nanocomposite (sample b) and pure CNTs measured at 10 A·g⁻¹ using 6 mol·L⁻¹ KOH as the electrolyte.

resistance and charge transfer resistance values were 0.24 and 0.53 Ω , respectively. The cycling performance of the Ni₂P@CNT nanocomposites at 10 A·g⁻¹ was further investigated as shown in Figs. 4(d) and S4. The Ni₂P@CNT nanocomposites retained 84% of their initial specific capacitance even after 5000 cycles; thus, they have excellent cycling stability.

The rate performance of the Ni₂P@CNT nanocomposite electrode was further investigated as shown in Fig. 5(a). The Ni₂P@CNT nanocomposite had excellent electrochemical performance and maintained a high electrochemical of 90% even at a current of 10 A·g⁻¹. The specific capacitance was almost constant even after charge-discharge. This result further indicates the great potential of this material for various applications. The cathodic and anodic current responses of the Ni₂P@CNT nanocomposite were detected between 0 and 0.6 V. Obeying the power law, $i = av^b$ [42,43], the b values of 0.8322 and 0.8473 were obtained for the cathodic and anodic current responses, respectively (Fig. 5(b)). These results suggest that the current was surface controlled and that the

dominant electrochemical reaction in the Ni₂P@CNT electrode was the capacitive effect. The total capacitance of the electrode material consisted of the following two components: 1) the capacitance behavior, which was generated by ion adsorption/desorption and redox reactions independent of the current density or scanning rate, and 2) the diffusion process, which was caused by ion insertion into both the electrode material and electrolyte. As shown in Fig. 5(c), the capacitive contribution was approximately 53.9% at the scan rate of 5 mV·s⁻¹. Intriguingly, as shown in Fig. 5(d), the specific capacitance contribution displayed a gradual upward trend from 53.9% to 83.2% when the scan rate increased from 5 to 100 mV·s⁻¹. The increased capacitive contribution would be beneficial for fast charge transfer.

3.5 Electrochemical characterization for the assembled ASCs

Ni₂P@CNT//AC devices were assembled by using the optimal Ni₂P@CNT nanocomposite as the positive

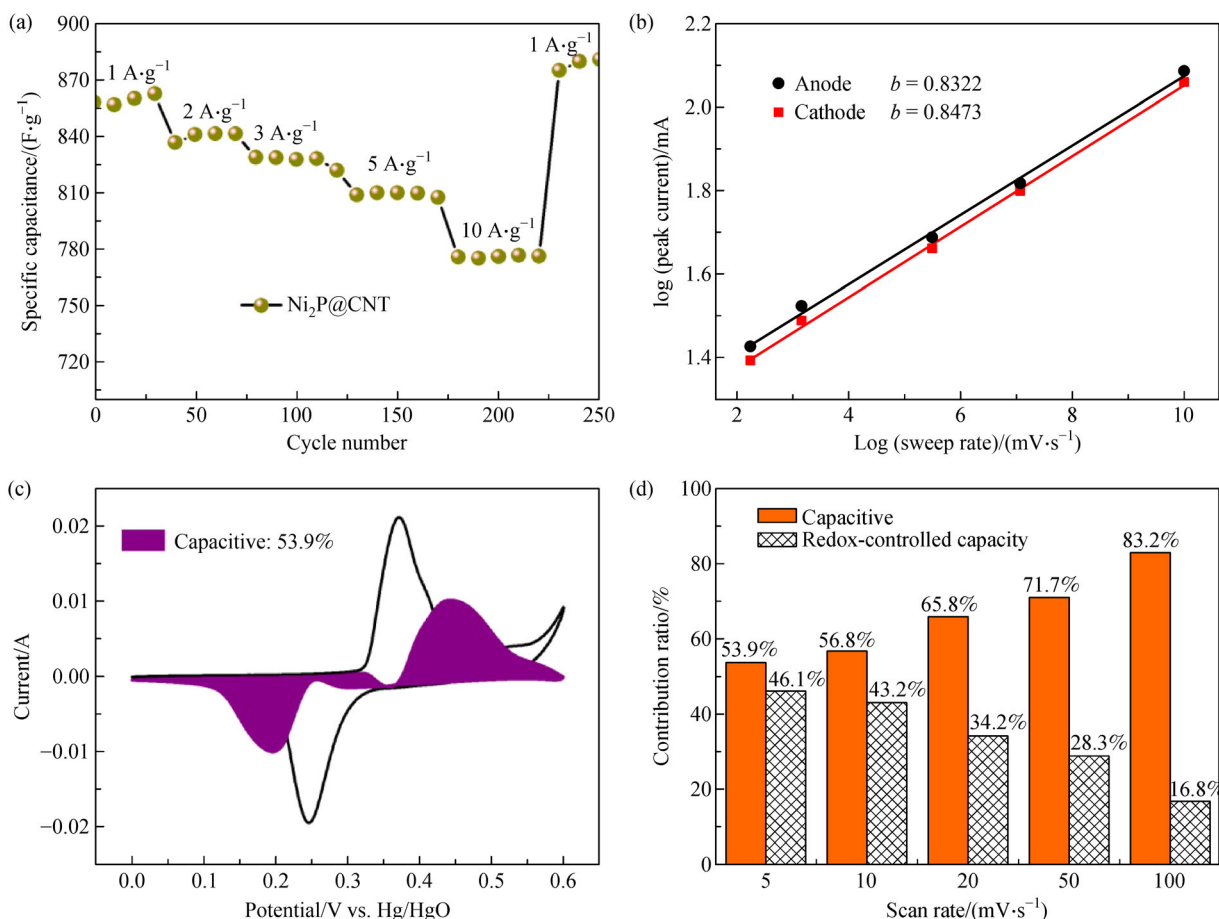


Fig. 5 (a) Cyclic test under continuous transformation conditions; (b) logarithmic plots of the peak current vs. the logarithm of the scan rate; (c) comparison of the capacitive contribution and the redox-controlled contribution at a scan rate of 5 mV·s⁻¹; (d) capacitive and redox-controlled contribution ratios at different scanning rates. All the tests were based on the optimal Ni₂P@CNT nanocomposites (sample b).

electrode (sample b) and AC as the negative electrode material to further evaluate the potential applications of the resultant Ni₂P@CNT nanocomposites in practice. As shown in Fig. 6(a), the potential windows of the Ni₂P@CNT nanocomposite and AC ranged from 0 to 0.6 V and -1 to 0 V, respectively, which led to the extended window of 0–1.6 V in the ASC. As displayed in Fig. 6(b), the CV curves of the ASC were tested in the range of 10–100 mV·s⁻¹. The similar shapes of these curves indicate that the assembled ASC has good rate performance. Based on the GCD curves (Fig. 6(c)), the specific capacitance of the ASC can be calculated as 100.3, 91.8, 80.1, 72.0 and 59.1 F·g⁻¹ at the current densities of 0.5, 1.0, 2.0, 3.0 and 5.0 A·g⁻¹, respectively. Moreover, the EIS

measurement results are shown in Fig. 6(d). We fitted the equivalent circuit diagram through the analysis of the EIS spectrum. The semicircle diameter in the high-frequency region represents the charge transfer resistance ($R_{ct} = 0.013 \Omega$) at the electrode material/electrolyte interface. The bulk resistance of the system, including the solid electrolyte and internal resistance of the electrode, was calculated as 1.2 Ω . Figure 6(e) shows the Ragone plots of the assembled Ni₂P@CNT//AC device. The results show that the energy density of Ni₂P@CNT//AC could reach up to 33.5 W·h·kg⁻¹ with a power density of 387.5 W·kg⁻¹, which is higher than previously reported, as listed in Table 3. Furthermore, the assembled ASCs had excellent cycle performance with 99.5% capacitance retention after

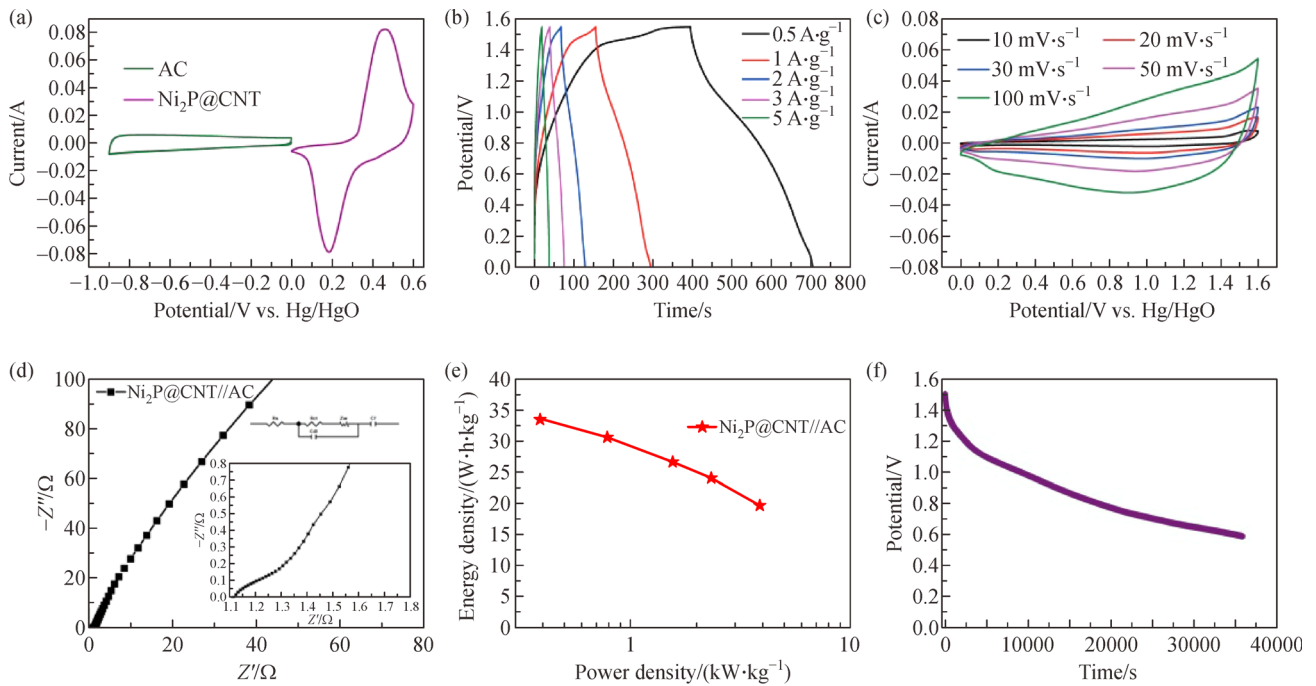


Fig. 6 Electrochemical performance of the assembled ASC based on Ni₂P@CNT//AC: (a) CV curves of Ni₂P@CNTs and AC electrodes at 50 mV·s⁻¹; (b) CV curves of Ni₂P@CNT//AC (sample b); (c) GCD curves at different current densities; (d) Nyquist plots of the Ni₂P@CNT//AC ASC; (e) Ragone plot of the Ni₂P@CNT//AC ASC. The inset is a picture of an LED light powered by two connected ASC devices; (f) Self-discharge characteristics of the assembled ASC device over 36000 s.

Table 3 Energy densities and powder densities of different transition metal phosphides in recent studies

Material	Method	Energy density/(W·h·kg ⁻¹)	Power density/(W·kg ⁻¹)	Ref.
Co ₂ P nanoflowers//graphene	Thermal decomposition	24	300	[51]
Ni ₂ P NS/NF//AC	Thermal decomposition	26	337	[52]
Ni ₂ P/Ni/C//AC	Thermal decomposition	32.02	700	[20]
NiCoP@NF//AC	Thermal decomposition	27	647	[53]
Fe ₂ O ₃ /Ni ₂ P	Thermal decomposition	29.8	400	[54]
MnO ₂ -CNT//AC	Hydrothermal	25	500	[55]
Ni ₂ P@CNT//AC	Microwave radiation	33.5	387.5	This work

3000 cycles (Fig. S3, cf. ESM). Additionally, the Ni₂P@CNT//AC device could successfully light three light emitting diode (LED) lights for 6 min and thus has excellent energy storage performance. Finally, the self-discharge characteristics of the Ni₂P@CNT//AC were studied at room temperature. As shown in Fig. 6(f), the maximum charging voltage of the ASC device was 1.5 V. Although the voltage sharply dropped at the beginning probably because of the decomposition of water [44,45], the potential could still stay at 0.6 V over a 10-h self-discharge period.

The superior electrochemical performance of the optimal Ni₂P@CNT nanocomposite (sample b) can be explained as follows. 1) The specific surface area and porosity of the samples were further studied by nitrogen adsorption/desorption test as shown in Fig. S2. The porous structure is beneficial to the transport and diffusion of electrolyte ions [46]. 2) The CNT provided an effective reaction site; thus, the electrolyte and materials had a large contact area. The large contact area reduced the loss in the energy transfer process and provided good cyclic performance [47]. 3) The metal phosphates had low redox potential and high specific capacitance. Hence, the Ni₂P@CNT nanocomposites had excellent power density and energy density [48,49]. 4) The optimal sample (sample b) had desirable morphology, which enabled the Ni₂P to uniformly grow on the surface of the CNTs. The synergistic effects of the CNTs with the Ni₂P nanoparticles improved the electrochemical property of the electrode [50].

4 Conclusions

In summary, Ni₂P@CNT nanocomposites with excellent energy storage performance were successfully obtained by an energy-efficient and ultrafast microwave synthesis method. The obtained Ni₂P@CNT nanocomposites exhibited a remarkable specific capacitance of 854 F·g⁻¹ at 1 A·g⁻¹ and showed high cycling stability with specific capacitance retention of 84% even after 5000 charge–discharge cycles at a current density of 10 A·g⁻¹. Furthermore, a Ni₂P@CNT//AC asymmetric supercapacitor device was assembled, which exhibited a high energy density of 33.5 W·h·kg⁻¹ with a power density of 387.5 W·kg⁻¹. We anticipated that our study of this microwave approach for the ultrafast nano-manufacturing of transition metal phosphides will open exciting opportunities for the creation of a wide range of electrode nanomaterials for supercapacitor applications.

Acknowledgements The authors would like to thank National Natural Science Foundation of China (Grant No. 21306124) for the financial support of this work and Haishun Du acknowledges the financial support from the China Scholarship Council (Grant No. 201708120052).

Electronic Supplementary Material Supplementary material is available

in the online version of this article at <https://doi.org/10.1007/s11705-020-2006-x> and is accessible for authorized users.

References

- Kong S Y, Cheng K, Ouyang T, Gao Y Y, Ye K, Wang G L, Cao D X. Facile dip coating processed 3D MnO₂-graphene nanosheets/MWNT-Ni foam composites for electrochemical supercapacitors. *Electrochimica Acta*, 2017, 226: 29–39
- Zhang N, Ding Y H, Zhang J Y, Fu B, Zhang X L, Zheng X F, Fang Y Z. Construction of MnO₂ nanowires@Ni_{1-x}Co_xO_y nanoflake core-shell heterostructure for high performance supercapacitor. *Journal of Alloys and Compounds*, 2017, 694: 1302–1308
- Li Y J, Ou-Yang W, Xu X T, Wang M, Hou S J, Lu T, Yao Y F, Pan L K. Micro-/mesoporous carbon nanofibers embedded with ordered carbon for flexible supercapacitors. *Electrochimica Acta*, 2018, 271: 591–598
- Li Y J, Zhu G, Huang H L, Xu M, Lu T, Pan L K. A N, S dual doping strategy via electrospinning to prepare hierarchically porous carbon polyhedra embedded carbon nanofibers for flexible supercapacitors. *Journal of Materials Chemistry. A, Materials for Energy and Sustainability*, 2019, 7(15): 9040–9050
- Xu X T, Liu Y, Wang M, Zhu C, Lu T, Zhao R, Pan L K. Hierarchical hybrids with microporous carbon spheres decorated three-dimensional graphene frameworks for capacitive applications in supercapacitor and deionization. *Electrochimica Acta*, 2016, 193: 88–95
- Liu Z, Zhang L, Wang R G, Poyraz S, Cook J, Bozack M J, Das S, Zhang X Y, Hu L B. Ultrafast microwave nano-manufacturing of fullerene-like metal chalcogenides. *Scientific Reports*, 2016, 6(1): 22503
- Lu Z, Chang Z, Zhu W, Sun X. Beta-phased Ni(OH)₂ nanowall film with reversible capacitance higher than theoretical Faradic capacitance. *Chemical Communications*, 2011, 47(34): 9651
- Xie J, Sun X, Zhang N, Xu K, Zhou M, Xie Y. Layer-by-layer beta-Ni(OH)₂/graphene nanohybrids for ultraflexible all-solid-state thin-film supercapacitors with high electrochemical performance. *Nano Energy*, 2013, 2(1): 65–74
- Muzaffar A, Ahamed M B, Deshmukh K, Thirumalai J. A review on recent advances in hybrid supercapacitors: design, fabrication and applications. *Renewable & Sustainable Energy Reviews*, 2019, 101: 123–145
- Zhang Q, Uchaker E, Candelaria S L, Cao G. Nanomaterials for energy conversion and storage. *Chemical Society Reviews*, 2013, 42(7): 3127–3171
- Wang Y, Song Y, Xia Y. Electrochemical capacitors: mechanism, materials, systems, characterization and applications. *Chemical Society Reviews*, 2016, 45(21): 5925–5950
- Arul N S, Han J I. Enhanced pseudocapacitance of NiSe₂/Ni(OH)₂ nanocomposites for supercapacitor electrode. *Materials Letters*, 2019, 234: 87–91
- Yu Z, Tetard L, Zhai L, Thomas J. Supercapacitor electrode materials: nanostructures from 0 to 3 dimensions. *Energy & Environmental Science*, 2015, 8(3): 702–730
- Zhang N, Li Y F, Xu J Y, Li J J, Wei B, Ding Y, Armorim I, Thomas

- R, Thalluri S M, Liu Y Y, et al. High-performance flexible solid-state asymmetric supercapacitors based on bimetallic transition metal phosphide nanocrystals. *ACS Nano*, 2019, 13(9): 10612–10621
15. Chen H C, Jiang S P, Xu B H, Huang C H, Hu Y Z, Qin Y L, He M X, Cao H J. Sea-urchin-like nickel-cobalt phosphide/phosphate composites as advanced battery materials for hybrid supercapacitors. *Journal of Materials Chemistry. A, Materials for Energy and Sustainability*, 2019, 7(11): 6241–6249
 16. Panneerselvam A, Malik M A, Afzaal M, O'Brien P, Helliwell M. The chemical vapor deposition of nickel phosphide or selenide thin films from a single precursor. *Journal of the American Chemical Society*, 2008, 130(8): 2420–2421
 17. Li X, Elshahawy A M, Guan C, Wang J. Metal phosphides and phosphates-based electrodes for electrochemical supercapacitors. *Small*, 2017, 13(39): 1701530
 18. Pang H, Wei C, Ma Y, Zhao S, Li G, Zhang J, Chen J, Li S. Nickel phosphite superstructures assembled by nanotubes: original application for effective electrode materials of supercapacitors. *Chem-PlusChem*, 2013, 78(6): 546–553
 19. Zhao Y, Zhao M, Ding X, Liu Z R, Tian H, Shen H H, Zu X T, Li S A, Qiao L. One-step colloid fabrication of nickel phosphides nanoplate/nickel foam hybrid electrode for high-performance asymmetric supercapacitors. *Chemical Engineering Journal*, 2019, 373: 1132–1143
 20. Hou S J, Xu X T, Wang M, Xu Y Q, Lu T, Yao Y F, Pan L K. Carbon-incorporated Janus-type Ni₂P/Ni hollow spheres for high performance hybrid supercapacitors. *Journal of Materials Chemistry. A, Materials for Energy and Sustainability*, 2017, 5(369): 19054–19061
 21. Jiang H, Zhao T, Li C, Ma J. Hierarchical self-assembly of ultrathin nickel hydroxide nanoflakes for high-performance supercapacitors. *Journal of Materials Chemistry*, 2011, 21(11): 3818–3823
 22. Liu M C, Kong L B, Kang L, Li X, Walsh F C, Xing M, Lu C, Ma X J, Luo Y C. Synthesis and characterization of M₃V₂O₈ (M = Ni or Co) based nanostructures: a new family of high performance pseudocapacitive materials. *Journal of Materials Chemistry. A, Materials for Energy and Sustainability*, 2014, 2(14): 4919–4926
 23. Shih Y L, Wu C L, Wu T Y, Chen D H. Electrochemical fabrication of nickel phosphide/reduced graphene oxide/nickel oxide composite on nickel foam as a high performance electrode for supercapacitors. *Nanotechnology*, 2019, 30(11): 115601
 24. Lv Z J, Zhong Q, Bu Y F. *In-situ* conversion of rGO/Ni₂P composite from GO/Ni-MOF precursor with enhanced electrochemical property. *Applied Surface Science*, 2018, 439: 413–419
 25. Zhang X, Han M M, Liu G Q, Wang G Z, Zhang Y X, Zhang H M, Zhao H J. Simultaneously high-rate furfural hydrogenation and oxidation upgrading on nanostructured transition metal phosphides through electrocatalytic conversion at ambient conditions. *Applied Catalysis B: Environmental*, 2019, 244: 899–908
 26. Wang J, Ciucci F. *In-situ* synthesis of bimetallic phosphide with carbon tubes as an active electrocatalyst for oxygen evolution reaction. *Applied Catalysis B: Environmental*, 2019, 254: 292–299
 27. Lin Y, Zhang J, Pan Y, Liu Y Q. Nickel phosphide nanoparticles decorated nitrogen and phosphorus co-doped porous carbon as efficient hybrid catalyst for hydrogen evolution. *Applied Surface Science*, 2017, 422: 828–837
 28. Xu J Y, Li J J, Xiong D H, Zhang B S, Liu Y F, Wu K H, Amorim I, Li W, Liu L F. Trends in activity for the oxygen evolution reaction on transition metal (M = Fe, Co, Ni) phosphide precatalysts. *Chemical Science (Cambridge)*, 2018, 9(14): 3470–3476
 29. Huang Y F, Chiueh P T, Kuan W H, Lo S L. Microwave pyrolysis of lignocellulosic biomass: heating performance and reaction kinetics. *Energy*, 2016, 100: 137–144
 30. Dong J Y, Lu G, Yue J S, Cheng Z M, Kang X H. Valence modulation in hollow carbon nanosphere/manganese oxide composite for high performance supercapacitor. *Applied Surface Science*, 2019, 480: 1116–1125
 31. Poyraz S, Zhang L, Schroder A, Zhang X Y. Ultrafast microwave welding/reinforcing approach at the interface of thermoplastic materials. *ACS Applied Materials & Interfaces*, 2015, 7(40): 22469–22477
 32. Tian Y R, Du H S, Zhang M M, Zheng Y Y, Guo Q P, Zhang H P, Luo J J, Zhang X Y. Microwave synthesis of MoS₂/MoO₂@CNT nanocomposites with excellent cycle stability for supercapacitor electrodes. *Journal of Materials Chemistry. C, Materials for Optical and Electronic Devices*, 2019, 7(31): 9545–9555
 33. Low J, Yu J, Jaroniec M, Wageh S, Al-Ghamdi A A. Heterojunction photocatalysts. *Advanced Materials*, 2017, 29(20): 1601694
 34. Wang Z J, Jin Z L, Yuan H, Wang G R, Ma B Z. Orderly-designed Ni₂P nanoparticles on g-C₃N₄ and UiO-66 for efficient solar water splitting. *Journal of Colloid and Interface Science*, 2018, 532: 287–299
 35. Xie S L, Gou J X. Facile synthesis of Ni₂P/Ni₁₂P₅ composite as long-life electrode material for hybrid supercapacitor. *Journal of Alloys and Compounds*, 2017, 713: 10–13
 36. Hosseini M G, Shahryari E. Synthesis. Characterization and electrochemical study of graphene oxide-multi walled carbon nanotube-manganese oxide-polyaniline electrode as supercapacitor. *Journal of Materials Science and Technology*, 2016, 32(8): 763–773
 37. Ghasem H M, Elham S. Anchoring RuO₂ nanoparticles on reduced graphene oxide-multi-walled carbon nanotubes as a high-performance supercapacitor. *Ionics*, 2019, 25(5): 2383–2391
 38. Yang X, Tian Y R, Sarwar S, Zhang M M, Zhang H P, Luo J J, Zhang X Y. Comparative evaluation of PPyNF/CoO_x and PPyNT/CoO_x nanocomposites as battery-type supercapacitor materials via a facile and low-cost microwave synthesis approach. *Electrochimica Acta*, 2019, 311: 230–243
 39. Bi Y H, Nautiyal A, Zhang H P, Luo J J, Zhang X Y. One-pot microwave synthesis of NiO/MnO₂ composite as a high performance electrode material for supercapacitors. *Electrochimica Acta*, 2017, 260: 952–928
 40. Zhao G Z, Li Y J, Zhu G, Shi J Y, Lu T, Pan L K. Biomass-based N, P, and S self-doped porous carbon for high performance supercapacitors. *ACS Sustainable Chemistry & Engineering*, 2019, 7(14): 12052–12060
 41. Han L, Huang H L, Li J F, Yang Z L, Zhang X L, Zhang D F, Liu X J, Xu M, Pan L K. Novel zinc-iodine hybrid supercapacitors with a redox iodide ion electrolyte and B, N dual-doped carbon electrode exhibit boosted energy density. *Journal of Materials Chemistry. A, Materials for Energy and Sustainability*, 2019, 7(42): 24400–

- 24407
42. Lou P, Cui Z, Jia Z, Sun J, Tan Y, Guo X. Monodispersed carbon-coated cubic NiP₂ nanoparticles anchored on carbon nanotubes as ultra-long-life anodes for reversible lithium storage. *ACS Nano*, 2017, 11(4): 3705–3715
 43. Sun L, Zhang Y, Zhang D Y, Zhang Y H. Amorphous red phosphorus nanosheets anchored on graphene layers as high performance anodes for lithium ion batteries. *Nanoscale*, 2017, 9(46): 18552–18560
 44. Chen L, Bai H, Huang Z, Li L. Mechanism investigation and suppression of self-discharge in active electrolyte enhanced supercapacitors. *Energy & Environmental Science*, 2014, 7(5): 1750–1759
 45. Barzegar F, Khaleed A A, Ugbo F U, Oyeniran K O, Momodu D Y, Bello A, Dangbegnon J K, Manyala N. Cycling and floating performance of symmetric supercapacitor derived from coconut shell biomass. *AIP Advances*, 2016, 6(11): 115306
 46. An C H, Wang Y J, Li L, Qiu F Y, Xu Y N, Xu C C, Huang Y N, Jiao F, Yuan H T. Effects of highly crumpled graphene nanosheets on the electrochemical performances of pseudocapacitor electrode materials. *Electrochimica Acta*, 2014, 133: 180–187
 47. Ding Y L, Alias H, Wen D S, Williams R A. Heat transfer of aqueous suspensions of carbon nanotubes (CNT nanofluids). *International Journal of Heat and Mass Transfer*, 2006, 49(1): 240–250
 48. Wu C, Kopold P, van Aken P A, Maier J, Yu Y. High performance graphene/Ni₂P hybrid anodes for lithium and sodium storage through 3D yolk-shell-like nanostructural design. *Advanced Materials*, 2017, 29(3): 1604015
 49. Lu Y, Tu J P, Xiong Q Q, Xiang J Y, Mai Y J, Zhang J, Qiao Y Q, Wang X L, Gu C D, Mao S X. Controllable synthesis of a monophasic nickel phosphide/carbon (Ni₅P₄/C) composite electrode via wet-chemistry and a solid-state reaction for the anode in lithium secondary batteries. *Advanced Functional Materials*, 2012, 22(18): 3927–3935
 50. Guang Z X, Huang Y, Chen X F, Sun X, Wang M Y, Feng X S, Chen C, Liu X D. Three-dimensional P-doped carbon skeleton with built-in Ni₂P nanospheres as efficient polysulfides barrier for high-performance lithium-sulfur batteries. *Electrochimica Acta*, 2019, 307: 260–268
 51. Chen X, Cheng M, Chen D, Wang R. Shape-controlled synthesis of Co₂P nanostructures and their application in supercapacitors. *ACS Applied Materials & Interfaces*, 2016, 8(6): 3892–3900
 52. Qu G, Cheng J, Li X, Yuan D, Chen P, Chen X, Wang B, Peng H. A fiber supercapacitor with high energy density based on hollow graphene/conducting polymer fiber electrode. *Advanced Materials*, 2016, 28(19): 3646–3652
 53. Lan Y Y, Zhao H Y, Zong Y, Li X H, Sun Y, Feng J, Wang Y, Zheng X T, Du Y P. Phosphorization boosts the capacitance of mixed metal nanosheet arrays for high performance supercapacitor electrodes. *Nanoscale*, 2018, 10(25): 11775–11781
 54. Wang D, Kong L B, Liu M C, Luo Y C, Kang L. An approach to preparing Ni-P with different phases for use as supercapacitor electrode materials. *Chemistry (Weinheim an der Bergstrasse, Germany)*, 2015, 21(49): 17897–17903
 55. Ochai-Ejeh F, Madito M J, Makgopa K, Rantho M N, Olaniyan O, Manyala N. Electrochemical performance of hybrid supercapacitor device based on birnessite-type manganese oxide decorated on uncapped carbon nanotubes and porous activated carbon nanostructures. *Electrochimica Acta*, 2018, 289: 363–375